Title	Dual-mode operation of DC-excited memory motors under flux regulation
Author(s)	Yu, C; Chau, KT
Citation	IEEE Transactions on Industry Applications, 2011, v. 47 n. 5, p. 2031-2041
Issued Date	2011
URL	http://hdl.handle.net/10722/155660
Rights	IEEE Transactions on Industry Applications. Copyright © IEEE

Dual-Mode Operation of DC-Excited Memory Motors Under Flux Regulation

Chuang Yu and K. T. Chau, *Senior Member, IEEE*

***Abstract*—The concept of memory is due to the fact that the magnetization level of permanent magnets (PMs) in the motor can be easily regulated by a temporary dc current pulse and then be memorized automatically. By incorporating this concept into the hybrid-field doubly salient PM (DSPM) motor, the resulting dc-excited memory motor can offer effective and efficient air-gap flux control. The purpose of this paper is to newly propose and implement dual-mode operation for the dc-excited memory motor. Namely, by regulating the magnetization level of the PMs, the motor can operate either under the DSPM mode or under the switched reluctance mode while maintaining similar operating performances. Both simulation and experimentation are used to verify the validity of the proposed dual-mode operation.**

***Index Terms*—Doubly salient permanent magnet (DSPM), dual-mode operation, flux mnemonic, memory motor, switched reluctance (SR).**

I. Introduction

DUE TO HIGH efficiency and high power density, permanent magnet (PM) motors have been widely accepted for industrial and vehicular applications [1], [2]. However, because of the fixed PM excitation, they cannot easily perform air-gap flux control, hence limiting their constant-power operation range. Different from many flux-weakening techniques relying on control strategies or motor structures to indirectly vary the air-gap flux [3], [4], the concept of memory, or called the concept of flux mnemonic, directly focuses on the regulation of PM excitation source. Such concept is derived from the fact that the magnetization level of PMs can be regulated by a temporary dc current pulse and then be memorized automatically after removing this current pulse. Instead of using the prevalent rare-earth PM materials, the traditional aluminum–nickel-cobalt (AlNiCo) PM is employed to realize the concept of memory due to its low coercivity and high remanence.

Manuscript received May 18, 2010; revised January 25, 2011; accepted May 9, 2011. Date of publication July 14, 2011; date of current version September 21, 2011. Paper 2010-EMC-155.R1, presented at the 2009 International Conference on Power Electronics and Drive Systems, Taipei, Taiwan, November 2–5, and approved for publication in the IEEE TRANSACTIONS ON INDUSTRY APPLICATIONS by the Electric Machines Committee of the IEEE Industry Applications Society. This work was supported by a research grant (Project HKU 710710E) of the Research Grants Council in the Hong Kong Special Administrative Region, China.

C. Yu was with the Department of Electrical and Electronic Engineering, The University of Hong Kong, Pokfulam, Hong Kong. He is now with Johnson Electric, Shatin N.T., Hong Kong (e-mail: chuangyu@eee.hku.hk).

K. T. Chau is with the Department of Electrical and Electronic Engineering, The University of Hong Kong, Pokfulam, Hong Kong (e-mail: ktchau@eee.hku.hk).

Color versions of one or more of the figures in this paper are available online at http://ieeexplore.ieee.org.

Digital Object Identifier 10.1109/TIA.2011.2161850

By introducing this memory concept into a conventional interior PM motor structure, the resulting memory motor utilizes the d-axis stator current flowing through the ac armature windings to perform flux regulation of PMs in the rotor [5]. Thus, this so-called ac-excited memory motor still suffers from the complicated vector control to decouple the stator current. In addition, its motor structure suffers from the lack of mechanical integrity and the possibility of demagnetization due to armature reaction.

Switched reluctance (SR) motors take the advantages of simple construction, fault tolerance, and mechanical robustness while suffering from relatively low efficiency and low power density [6]. By incorporating both the PMs and field windings into the stator of an SR motor, the resulting hybrid-field doubly salient PM (HF-DSPM) motor not only inherits the merits of both the SR motor and the PM motor but also offers flexible air-gap flux control [7], [8]. Based on the concept of memory and the HF-DSPM motor structure, the so-called dc-excited memory motor is developed in which a temporary dc current pulse is applied to the magnetizing windings so as to directly regulate the magnetization level [9].

Previous literature has addressed not only the basic generation and motoring operations but also the advanced flux-weakening operation of this dc-excited memory motor [10], [11]. Moreover, a qualitative comparison with other three types of PM motors and a quantitative comparison with the HF-DSPM motor have been conducted [12], which reveals that the dc-excited memory motor possesses a comparable power density to and much better flux-weakening capability than the traditional PM motors. Although this dc-excited memory motor is designed and implemented with relatively low power rating, it can be readily extended to high power rating for application to electric vehicles and wind power generation.

The idea of dual-mode operation is first introduced to handle open-circuit and short-circuit faults in memory motors [13]. The purpose of this paper is to propose and implement a new dual-mode operation of the dc-excited memory motor under flux regulation. The major contribution focuses on the formulation of dual-mode operation, the derivation of dual-mode operation using flux-current diagrams, the hardware and software implementations, and the simulation and experimental verification.

First, after the introduction of configuration, modeling, and inductance characteristics of the dc-excited memory motor, the definition of dual-mode operation will be given in Section II. Then, in Section III, by using the flux linkage versus current diagram, the torque production of the motor will be discussed. Section IV will address the control scheme of the dual-mode

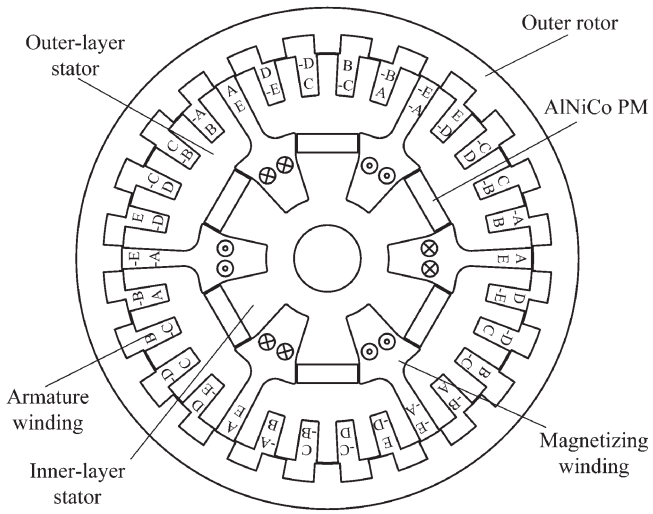

Fig. 1. Motor configuration.

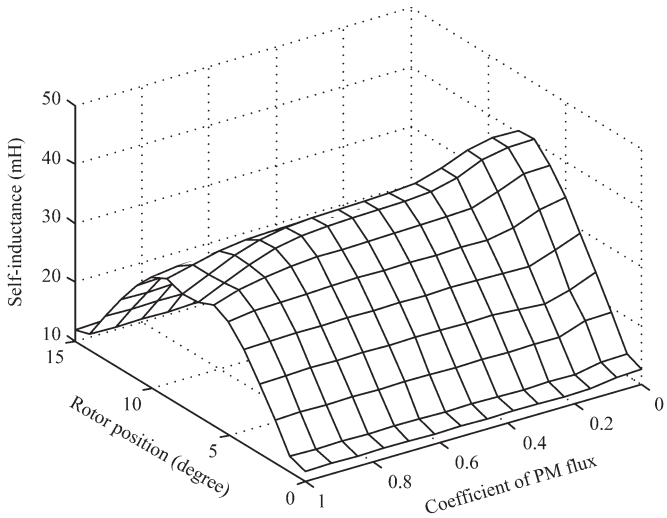

Fig. 2. Self-inductance graph with respect to rotor position and PM flux at rated armature current.

operation and present the operating performances of the motor under these two modes. Consequently, in Section V, experimental results will be given to verify the proposed dual-mode operation of the motor. Finally, a conclusion will be drawn in Section VI.

II. DC-Excited Memory Motor

A. Motor Configuration and Modeling

The configuration of the dc-excited memory motor is shown in Fig. 1, which adopts a five-phase outer-rotor double-layer-stator doubly salient topology. There are 24 salient poles in the outer rotor with no PMs or windings, thus offering high mechanical integrity. On the other hand, there are 30 salient poles in the outer-layer stator wound with armature windings. The compact inner-layer stator accommodates the AlNiCo PMs and the magnetizing windings. A temporary dc current pulse, controllable in both magnitude and direction, flows through the magnetizing windings to magnetize or demagnetize the PMs, hence achieving the flux regulation in the motor. The use of five phases rather than three phases is to enhance the torque smoothness and to provide the capability of fault tolerance. In addition, a higher number of phases can offer better starting performance. Notice that the use of two stator layers to accommodate the armature windings and PMs can enable the PMs immune from accidental demagnetization by armature reaction [9], [11].

Since the armature adopts concentrated windings with the coil span equal to the slot pitch, the mutual inductance between phase windings can be neglected. Moreover, since the magnetizing current is only applied in a very short time, there is negligible mutual inductance between armature windings and magnetizing windings. Therefore, the system modeling of the motor can be described by the following four equations.

1) Per-phase flux-linkage equation

$$\Psi = \kappa \Psi_{\rm PM} + Li. \tag{1}$$

2) Per-phase voltage equation

$$u = Ri + \frac{d\Psi}{dt}. \tag{2}$$

3) Per-phase electromagnetic torque equation

$$T_e = T_{\rm PM} + T_r = \kappa i \frac{d\Psi_{\rm PM}}{d\theta_m} + \frac{1}{2} i^2 \frac{dL}{d\theta_m}. \tag{3}$$

4) Mechanical motion equation

$$T_{\rm total} = T_L + J\frac{d\omega_m}{dt} + B\omega_m. \tag{4}$$

Ψ is the total flux linkage, $\Psi_{\rm PM}$ is the PM flux linkage, u is the terminal phase voltage, i is the phase current, R is the armature resistance, L is the armature self-inductance, T_e is the electromagnetic torque per phase, $T_{\rm PM}$ is the PM torque component per phase, T_r is the reluctance torque component per phase, $T_{\rm total}$ is the total output torque of five phases, T_L is the load torque, θ_m is the mechanical rotor position, $\omega_m = d\theta_m/dt$ is the mechanical angular velocity, J is the rotor inertia, B is the viscous coefficient, and κ is the coefficient of PM flux linkage due to flux regulation, $\kappa \in [0, 1]$. It should be noted that the use of torque equation to represent the motor is valid as far as the magnetic saturation is not severe. From these equations, it can be easily found that, for the maximum torque/current control and the maximum efficiency control, the optimal choice is to operate the motor under its full PM magnetization level, namely, $\kappa = 1$.

B. Self-Inductance

It is well known that the PM flux linkage is varying under the flux regulation, which is denoted by κ in the aforementioned equations. In addition, the self-inductance of armature windings is also varying due to the variation of flux saturation in the iron core. When κ varies from one to zero, where the PM flux linkage decreases from its maximum value to zero, the self-inductance gradually increases with κ. Fig. 2 shows a

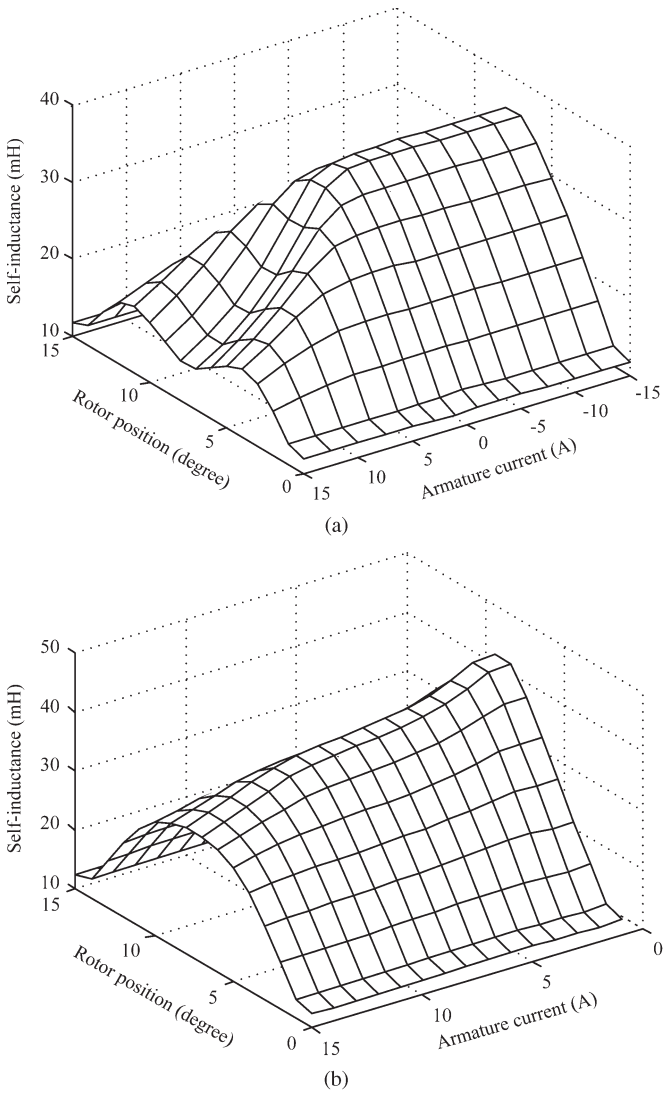

Fig. 3. Self-inductance graphs with respect to rotor position and armature current at different PM magnetization levels. (a) $\kappa = 1$. (b) $\kappa = 0$.

3-D graph of self-inductance of the phase-A winding with respect to the rotor position and the coefficient of PM flux at the rated armature current of $+5$ A, which indicates that the amplitude of self-inductance increases from about 30 to 40 mH when κ varies from one to zero.

Moreover, the self-inductance graphs of the phase-A winding with respect to the rotor position and the armature current at different PM magnetization levels of $\kappa = 1$ and $\kappa = 0$ are shown in Fig. 3. It should be noted that, since there is no PM excitation at $\kappa = 0$ and only a positive armature current should be applied during motoring, Fig. 3(b) shows the self-inductance at the positive currents only. It further confirms that the self-inductance at $\kappa = 0$ is larger than that at $\kappa = 1$.

C. Definition of Dual-Mode Operation

According to the torque (3) and the corresponding theoretical waveforms of $\Psi_{\rm PM}$ and L, there are two operation modes to make a unidirectional torque all the time. First, as shown in Fig. 4(a), a bipolar rectangular armature current is used, in

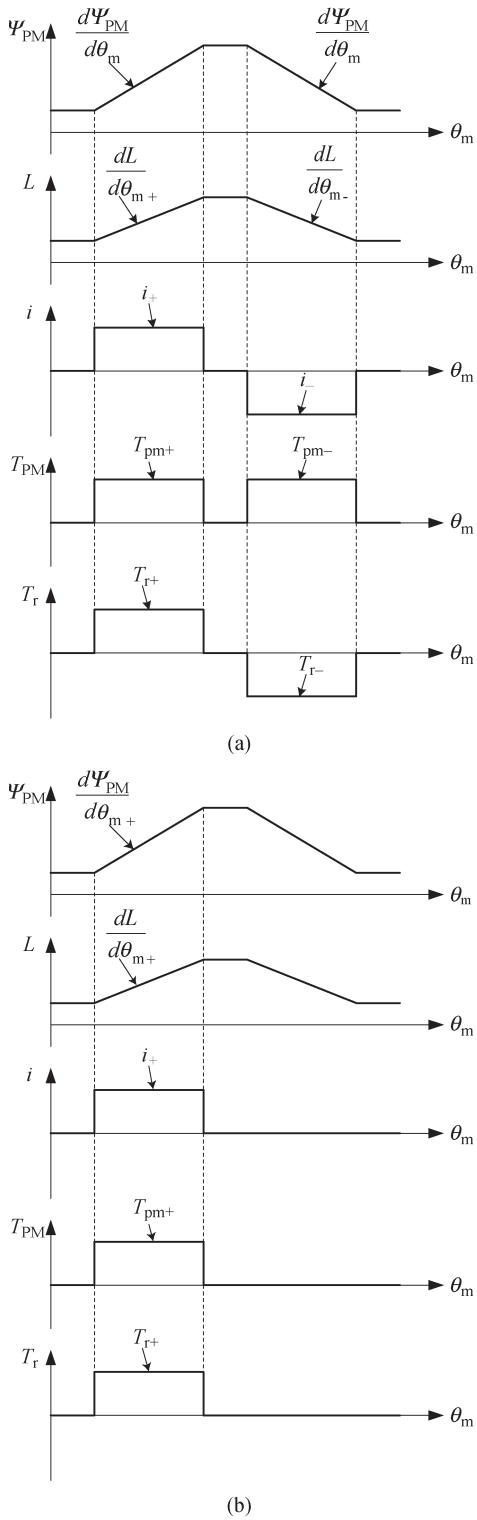

Fig. 4. Operation waveforms under different modes. (a) DSPM mode. (b) SR mode.

which a positive current is applied when $\Psi_{\rm PM}$ and L increase, whereas a negative current is applied when they decrease. As a result, the PM torque becomes the dominant torque component, while the reluctance one is a pulsating torque with zero average value. This mode of operation is adopted in the DSPM motor, so-called the DSPM mode of the dc-excited memory motor. Second, as shown in Fig. 4(b), a unipolar rectangular armature

current is used, in which only the positive current is applied in the period of increasing $\Psi_{\rm PM}$ and L. Since the period with decreasing $\Psi_{\rm PM}$ and L is not utilized, the torque density is sacrificed. This mode of operation is adopted in the SR motor, so-called the SR mode of the dc-excited memory motor.

Accordingly, the per-phase torque equation of the dc-excited memory motor can be rewritten as

$$T_e = \begin{cases} T_{\rm PM+} + T_{\rm PM-} + T_{r+} + T_{r-} & \text{DSPM mode} \\ T_{\rm PM+} + T_{r+} & \text{SR mode} \end{cases}$$
$$= \begin{cases} \kappa i_+ \frac{d\Psi_{\rm PM}}{d\theta_m}_+ + \kappa i_- \frac{d\Psi_{\rm PM}}{d\theta_m}_- \\ \quad + \frac{1}{2} i_+^2 \frac{dL}{d\theta_m}_+ + \frac{1}{2} i_-^2 \frac{dL}{d\theta_m}_- & \kappa \geq \kappa_0, \text{ DSPM mode} \\ \kappa i_+ \frac{d\Psi_{\rm PM}}{d\theta_m}_+ + \frac{1}{2} i_+^2 \frac{dL}{d\theta_m}_+ & \kappa < \kappa_0, \text{ SR mode} \end{cases} \tag{5}$$

where the subscript "+" or "−" denotes that the corresponding variables are in the increasing period or in the decreasing period of $\Psi_{\rm PM}$ and L, respectively, and κ_0 is the κ value at the critical transition point between two modes.

From the analysis of self-inductance, it reveals that the weakening of PM magnetization levels will reduce the PM torque but will increase the self-inductance and hence the reluctance torque. Hence, the reduction of PM torque can be compensated by the increase of reluctance torque, leading to the possibility of maintaining the total output torque. Therefore, according to the value of κ, the dual-mode operation of the dc-excited memory motor can be further divided into four stages.

1) When $\kappa = 1$, the PMs are in their full magnetization level so that the motor totally works as a DSPM motor.
2) When $\kappa_0 \leq \kappa < 1$, the PMs are partially demagnetized, and the PM torque is still the dominant torque component so that the motor retains operating as a DSPM motor.
3) When $0 < \kappa < \kappa_0$, the PMs are further demagnetized, resulting in a further reduction of PM torque but with a significant increase of reluctance torque so that the motor operates as an SR motor to fully utilize the reluctance torque.
4) When $\kappa = 0$, the PMs are completely demagnetized so that the motor thoroughly becomes an SR motor with only the reluctance torque contributed.

By using the finite-element method (FEM), the magnetic field of the motor at the same armature current under the DSPM mode at $\kappa = 1$ and the SR mode at $\kappa = 0$ is analyzed as shown in Fig. 5. According to the operation principles of DSPM motors and SR motors, four and two phases are conducted simultaneously under these two modes, respectively. Moreover, the corresponding air-gap flux density distributions are shown in Fig. 6. It can be found that, with the same current excitation, the magnitude of air-gap flux density under the SR mode is lower than that under the DSPM mode.

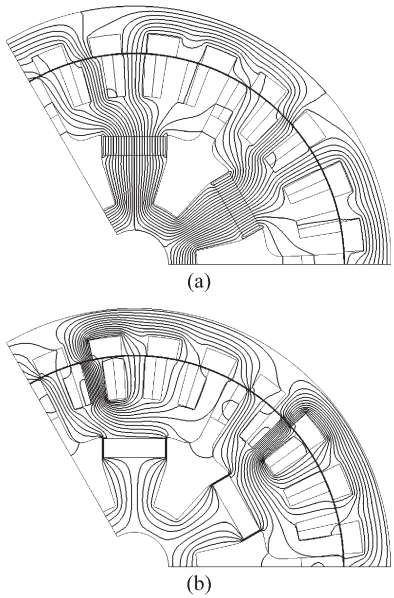

Fig. 5. Magnetic field distributions at the same armature current under different operation modes. (a) DSPM mode ($\kappa = 1$). (b) SR mode ($\kappa = 0$).

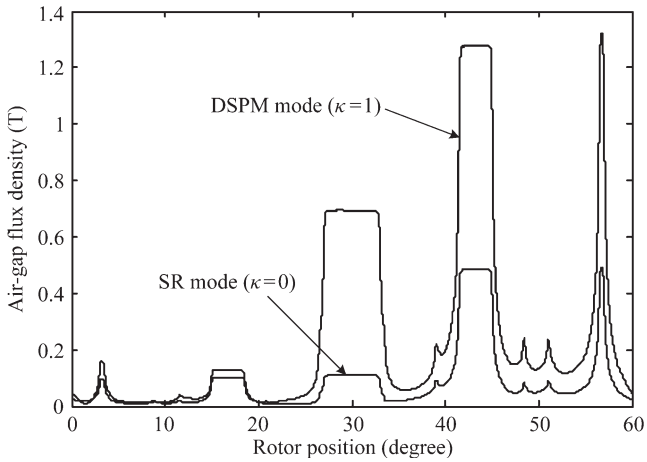

Fig. 6. Air-gap flux density distributions under DSPM mode ($\kappa = 1$) and SR mode ($\kappa = 0$).

III. Torque Production

A. Flux-Linkage–Current Diagram

The flux linkage versus current ($\Psi - i$) diagram has been widely used to analyze the performance of SR motors [6]. Moreover, it has been extended to other types of motors to predict their output torques and to facilitate direct comparisons with the SR motor [14]–[16]. Therefore, it is further extended to analyze the torque production of the dc-excited memory motor under different operation modes.

The $\Psi - i$ diagram plots the variation of Ψ versus i, based on which the instantaneous torque per phase $T_{\rm inst}$ is given by

$$T_{\rm inst} = \left.\frac{\partial W'}{\partial \theta_m}\right|_{i=\text{constant}} \tag{6}$$

where W' is the coenergy defined as

$$W' = \int_0^i \Psi di. \tag{7}$$

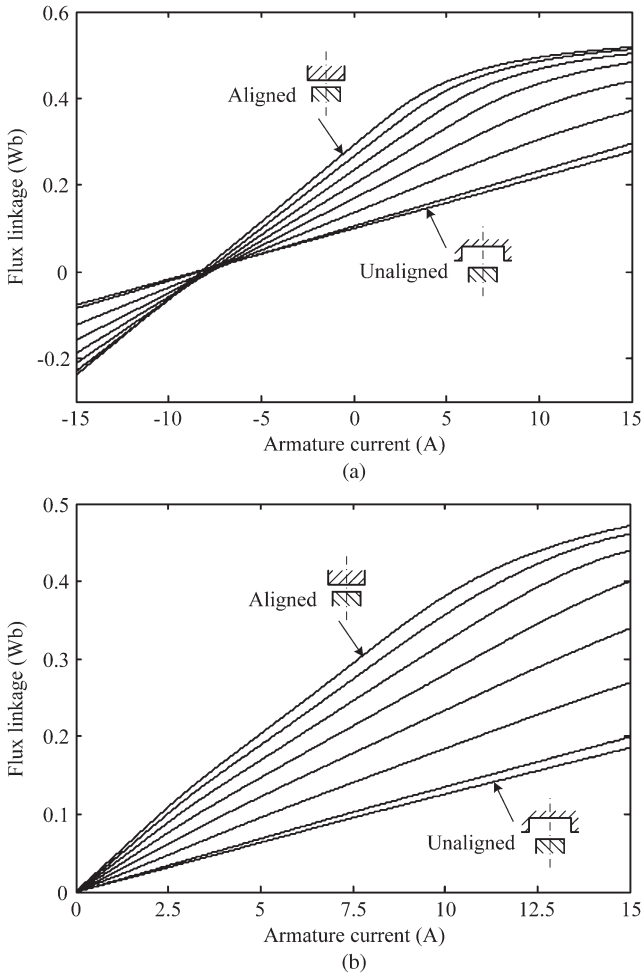

Fig. 7. Flux-linkage–current diagrams under different operation modes. (a) DSPM mode ($\kappa = 1$). (b) SR mode ($\kappa = 0$).

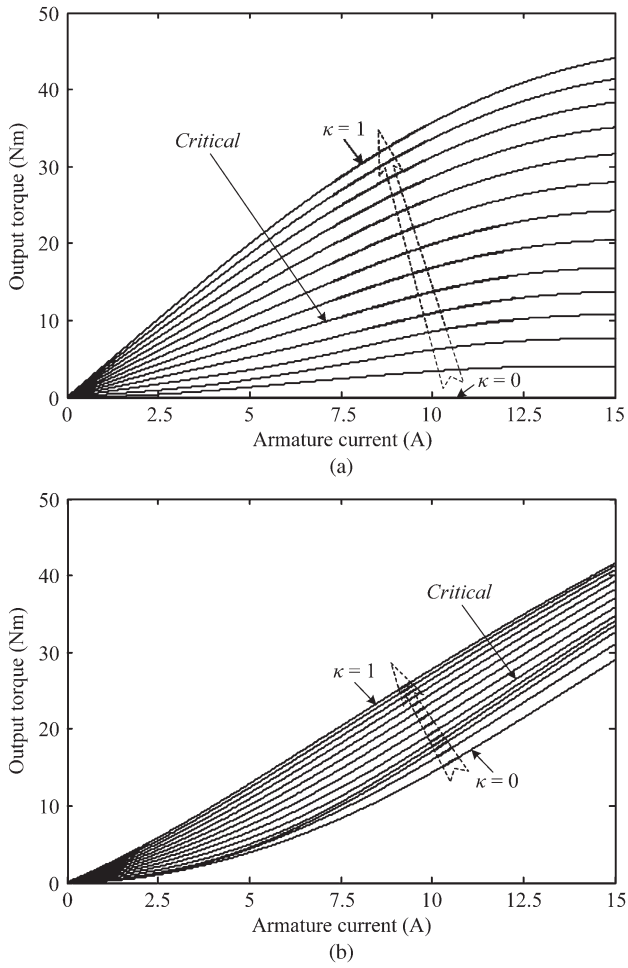

Fig. 8. Output torque curves using different control strategies. (a) DSPM current control. (b) SR current control.

Rather than directly integrating the instantaneous torque, the average torque $T_{\rm av}$ at a current I_0 can be obtained by

$$T_{\rm av} = \frac{mN_r}{2\pi} W_0 \tag{8}$$

where m is the number of phases, N_r is the number of rotor poles, and W_0 is the mechanical energy converted from electrical energy per stroke which is equal to the area in the $\Psi - i$ diagram enclosed between the unaligned $\Psi - i$ curve, the aligned $\Psi - i$ curve, and the vertical line of I_0.

By using the FEM, the two $\Psi - i$ diagrams of the dc-excited memory motor under the DSPM mode at $\kappa = 1$ and the SR mode at $\kappa = 0$ are shown in Fig. 7, where the aligned and unaligned positions between the stator pole and the rotor pole are both indicated. It can be observed that, under the DSPM mode, due to the PM excitation, the flux saturation in the iron core at the positive current direction is reached earlier and the flux attenuation in the iron core at the negative current direction is reached later than those under the SR mode. In addition, unlike the ideal $\Psi - i$ diagram of a DSPM motor, which involves only the first and second quadrants [15], the $\Psi - i$ diagram of this motor under the DSPM mode extends to the third quadrant because of the presence of large negative armature reaction. Notice that the $\Psi - i$ diagrams with other κ values under the two modes are similar to those shown in Fig. 7.

Therefore, the average output torque of the motor under different operation modes can be readily obtained by using (8). Fig. 8 shows the output torque versus armature current curves of the motor using the DSPM current control strategy (bipolar current applied) and the SR current control strategy (unipolar current applied) with κ varying from zero to one. It can be found that, when κ is approaching one, the torque–current curves are becoming more and more linear because the PM torque component is dominating, whereas when κ is close to zero, they are squarely related since the reluctance torque component becomes dominant.

B. Critical Transition Point

For the dual-mode operation of the motor, it is important to determine the critical transition point between the DSPM mode and the SR mode so that an appropriate current control strategy can be adopted to produce the output torque as large as possible at a given κ. By equating the output torque expressions of these two modes in (5), κ_0 should satisfy

$$T_{\rm PM-} + T_{r-}|_{\kappa=\kappa_0} = \kappa_0 i_- \frac{d\Psi_{\rm PM}}{d\theta_m}_{-} + \frac{1}{2} i_-^2 \frac{dL}{d\theta_m}_{-} = 0. \tag{9}$$

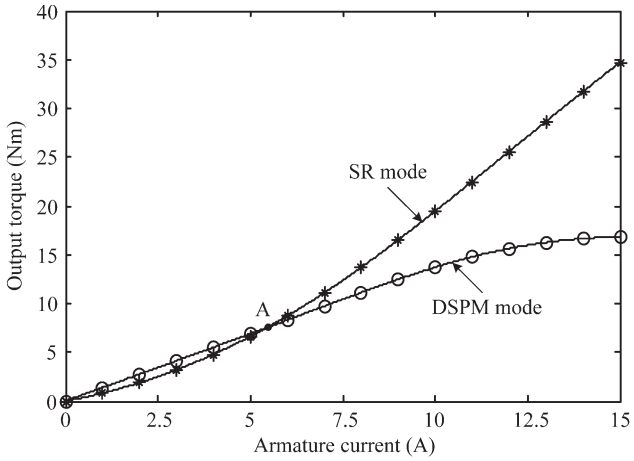

Fig. 9. Output torque curves under different operation modes at critical transition point.

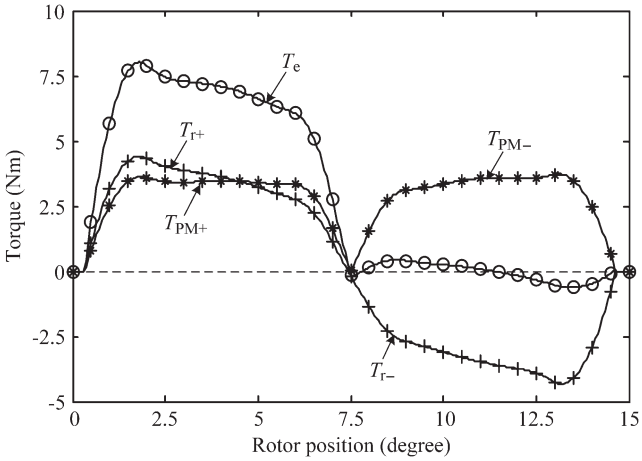

Fig. 10. Static torque and its component waveforms at critical transition point.

In order to determine κ_0, the motor is first assumed to work around its rated condition. Then, a graphical searching approach is employed. Namely, at each value of κ (varying from zero to one), the output torque curve in Fig. 8(a) is compared with that in Fig. 8(b) so as to identify which two curves have the same torque value when the armature current is nearby its rated value of 5 A. The resulting two critical curves are identified in Fig. 8 and then shown in Fig. 9 in which (9) is satisfied with $\kappa_0 = 0.385$ and $i_- = 5.5$ A as denoted by point A.

Consequently, when $i_- = 5.5$ A, the static torque and its component waveforms at the critical transition point are shown in Fig. 10, which reveals that the PM torque and the reluctance torque balance out in the second half-stroke, hence further confirming the validity of (9) at the critical PM magnetization level. Above this level, the dc-excited memory motor should operate under the DSPM mode, whereas below this level, the motor should operate under the SR mode.

C. Equivalent Output Torque

In addition to the critical transition point, another concern is to determine the values of armature current under different operation modes so as to produce an equivalent output torque.

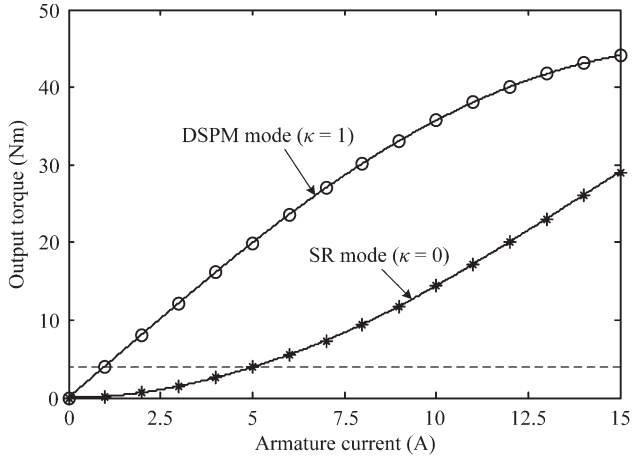

Fig. 11. Equivalent output torque curves under different operation modes.

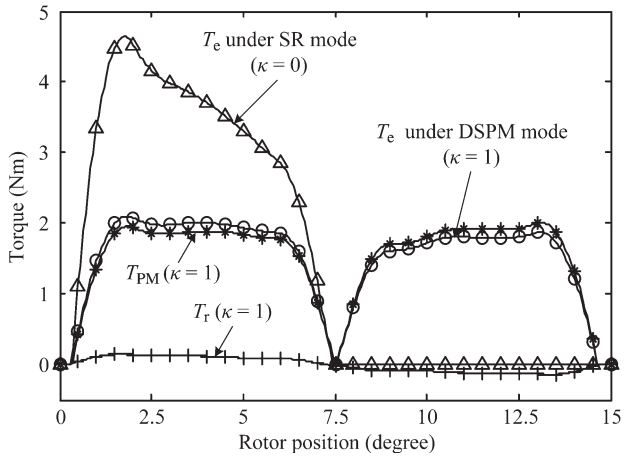

Fig. 12. Equivalent static torque waveforms under different operation modes.

Based on Fig. 8, the torque–current curves under the DSPM mode at $\kappa = 1$ and the SR mode at $\kappa = 0$ are redrawn in Fig. 11, which reveals that an armature current of 1 A under the DSPM mode and an armature current of 5 A under the SR mode produce an equivalent output torque of about 4 N · m as denoted by the dashed line. The corresponding static torque waveforms under different modes are shown in Fig. 12. It can be found that the area under the static torque waveform (marked with triangles) at the SR mode is approximately equal to the area under the waveform (marked with circles) at the DSPM mode, hence confirming that their average output torques over one stroke are equivalent.

IV. Dual-Mode Operation

A. Control Scheme

Fig. 13 shows the control scheme for the dual-mode operation of the dc-excited memory motor, which can be divided into five parts: the magnetizing controller, the magnetizing inverter, the armature controller, the armature inverter, and the motor.

In order to produce a temporary magnetizing or demagnetizing current pulse to switch between two operation modes, the magnetizing inverter consists of a dc/dc converter and an H-bridge inverter, where the former functions to control the

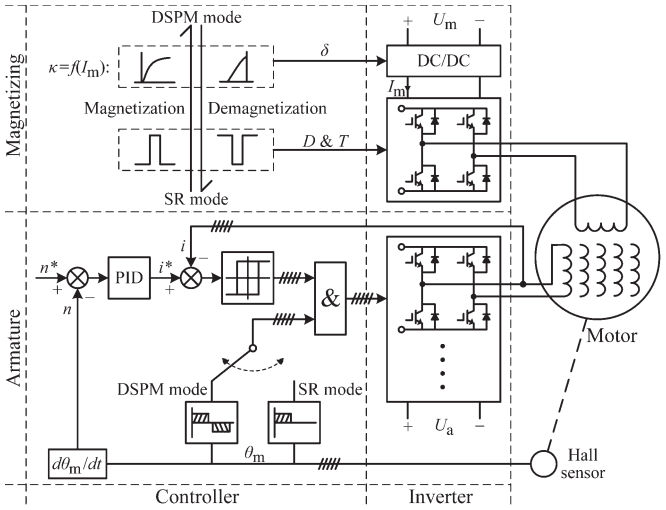

Fig. 13. Control scheme for dual-mode operation.

magnitude I_m of the current pulse and the latter serves to control the direction D and duration T of the current pulse.

Due to the nonlinearity of both the magnetization and demagnetization curves of the AlNiCo PMs, the relationship between κ and I_m is experimentally determined in advance and then stored as a lookup table for online use, which ensures that a complete demagnetization followed by a remagnetization for PMs is avoided when changing the value of κ. Accordingly, the duty cycle δ of the dc/dc converter is adjusted to produce the desired value of I_m. The value of T is simply the minimum duration to accomplish the magnetization or demagnetization process, which is not strictly controlled.

For the armature controller, it adopts a conventional dual-closed-loop control scheme, where the outer speed loop adopts a PID regulator to perform speed control, and the inner current loop uses a hysteresis regulator to perform current chopping control [17]. By comparing the speed command with the actual speed, the armature current command is resulted. Then, by comparing the current command with the actual current, the hysteresis regulator signal is generated. By logically combining the hysteresis regulator signal with the phase conduction signal, which depends on the mode of operation, the firing signal of each power switch in the armature inverter can be obtained.

Apart from the additional inverter for the magnetizing winding, the proposed motor drive needs a more complicated inverter for the armature winding and desires a more complex control circuit. First, in order to consolidate a conventional half-bridge inverter used for the DSPM motor drive and a conventional asymmetric half-bridge inverter used for the SR motor, the full-bridge inverter topology is adopted to power the armature winding. Second, additional sensing and conditioning circuits are required to estimate the air-gap flux and hence the value of κ so as to determine which operation mode should be adopted [11].

B. Operating Performance

For exemplification, the dc-excited memory motor operates under the DSPM mode at $\kappa = 1$ and the SR mode at $\kappa = 0$.

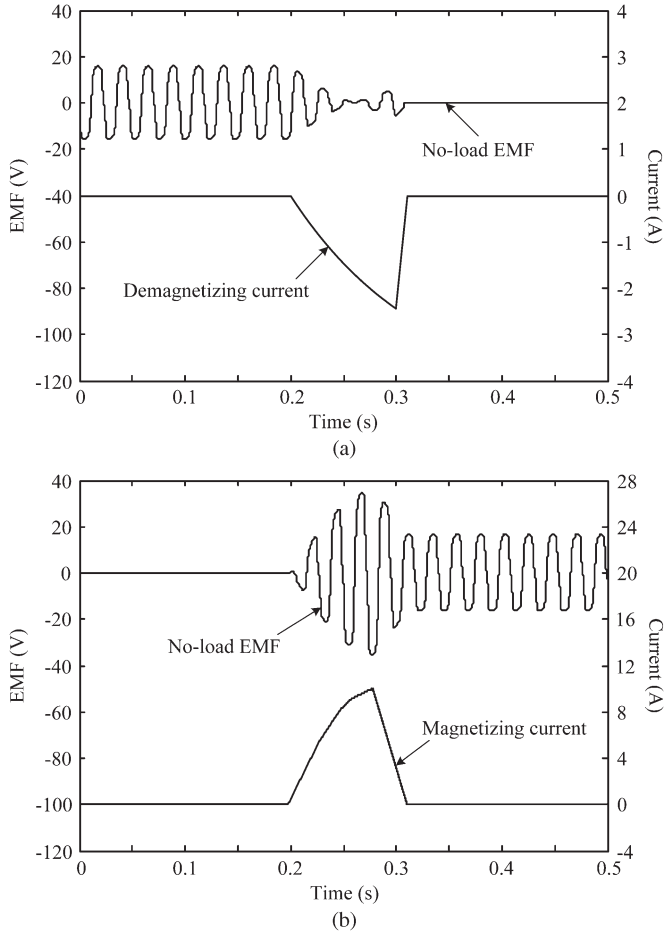

Fig. 14. Simulated transient responses of no-load EMF during mode transitions at 100 r/min. (a) DSPM mode to SR mode. (b) SR mode to DSPM mode.

Fig. 14 shows the simulated transient responses of the no-load electromotive force (EMF) at the speed of 100 r/min during two mode transitions, namely, from the DSPM mode to the SR mode and vice versa. The corresponding duration of current pulse needs only about 0.1 s. It can be observed that the PMs can be completely demagnetized by using a negative current pulse with a magnitude of 2.4 A so as to activate the SR mode, whereas the PMs can be completely remagnetized by using a positive current pulse with a magnitude of 10 A so as to reactivate the DSPM mode.

In addition, operating performances of the motor under the DSPM mode and the SR mode are assessed as shown in Figs. 15 and 16, respectively. When the motor starts from standstill to 400 r/min, the transient responses of rotor speed and armature current are shown in Figs. 15(a) and 16(a). They reveal that, under both operation modes, the motor exhibits a fast speed response to reach the speed command without overshoot and steady-state error. Moreover, they confirm that the bipolar armature current is applied under the DSPM mode while the unipolar armature current is applied under the SR mode. On the other hand, the steady-state waveforms of output torque and armature current are shown in Figs. 15(b) and 16(b). It can be found that the armature current of 1.2 A under the DSPM mode and that of 5.5 A under the SR mode produce the same output torque of about 5 N · m, which well agrees with the theoretical

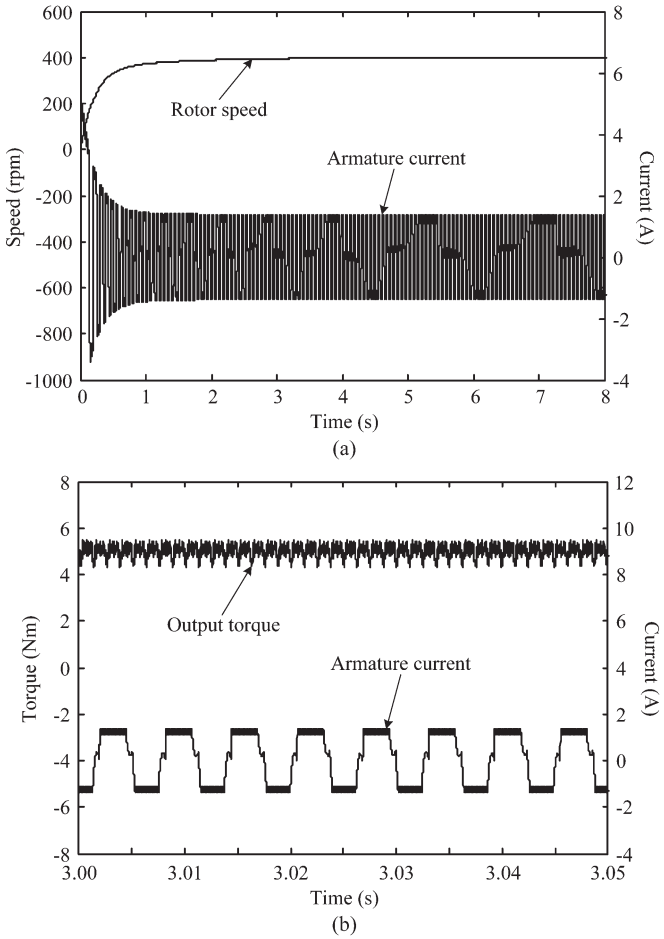

Fig. 15. Simulated operating performances under DSPM mode. (a) Transient responses during startup. (b) Steady-state waveforms at 400 r/min.

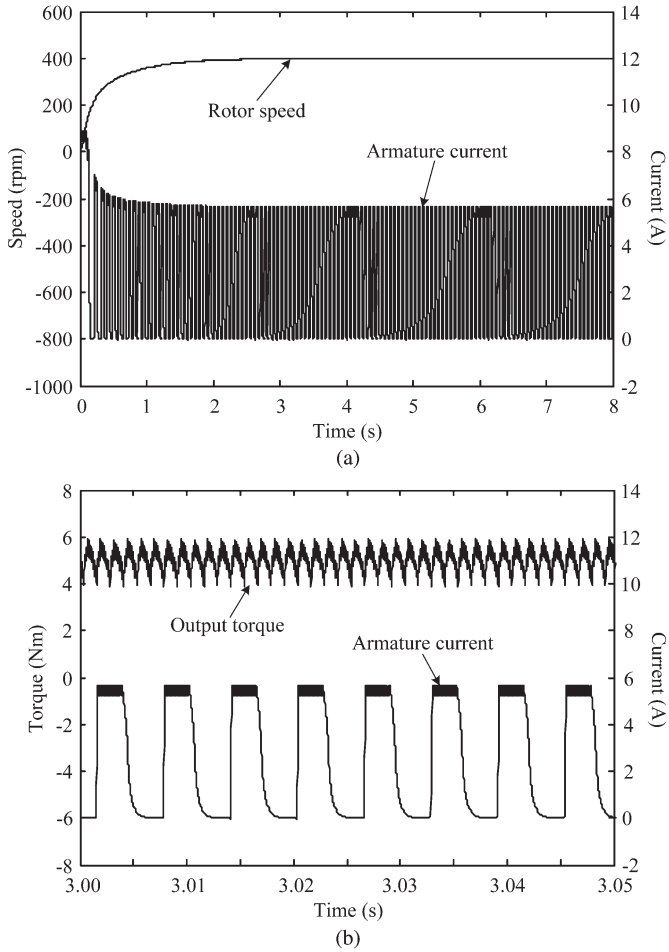

Fig. 16. Simulated operating performances under SR mode. (a) Transient responses during startup. (b) Steady-state waveforms at 400 r/min.

prediction shown in Fig. 11. Furthermore, it can be observed that the output torque ripple under the SR mode is larger than that under the DSPM mode, which is due to its feature of half-stroke torque production.

V. Experimental Verification

In order to experimentally verify the proposed dual-mode operation of the dc-excited memory motor, a motor prototype is built as shown in Fig. 17(a), where the stator, rotor, PM, armature winding, and magnetizing winding are all marked as similar to that in Fig. 1. It is then coupled with a dc dynamometer via a dynamic torque transducer as shown in Fig. 17(b). The key design data of the prototype are summarized in Table I.

First, the transient responses of the no-load EMF at the speed of 100 r/min during two mode transitions are measured as shown in Fig. 18. It can be found that the measured responses well agree with the simulated responses as shown in Fig. 14. It also confirms that a negative current pulse with $I_m = 2.4$ A and a positive current pulse with $I_m = 10$ A can successfully switch between two modes of operation.

Second, under the DSPM mode and the SR mode, the transient responses of rotor speed and armature current during startup from standstill to 400 r/min, and the steady-state

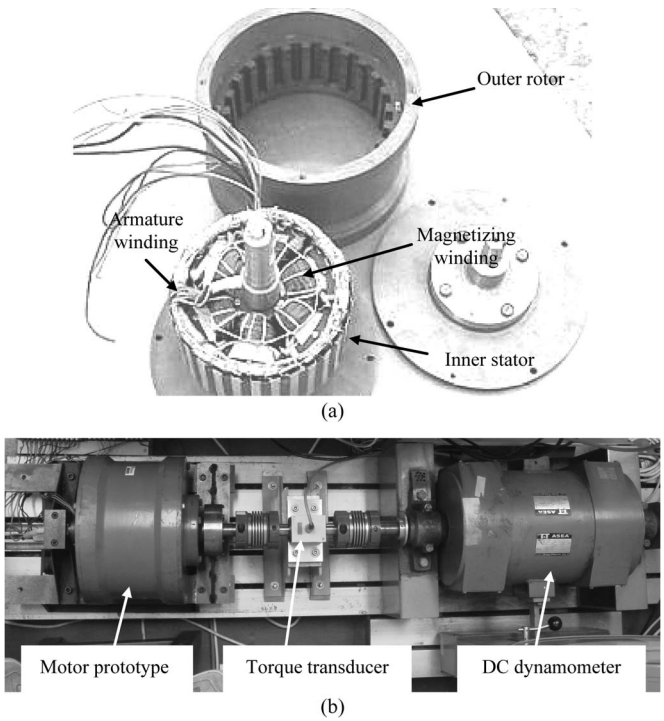

Fig. 17. Experimental setup. (a) Motor prototype. (b) Test bed.

TABLE I
KEY DESIGN DATA

Rated power	942 W
Rated torque	15 Nm
Rated speed	600 rpm
Speed range	0~2000 rpm
Stator outside diameter	220.0 mm
Rotor inside diameter	221.2 mm
Rotor outside diameter	270.0 mm
Stack length	80.0 mm
Armature winding turns	360×5
Magnetizing winding turns	1500
Armature winding mass	0.37×5 kg
Magnetizing winding mass	1.12 kg
Rotor pole arc	7 degree
Stator pole arc	6 degree
PM material	Alnico 5DG
PM dimensions (width × thickness)	33×10 mm
PM remanent flux density	1.3 T
PM coercive force	56 kA/m

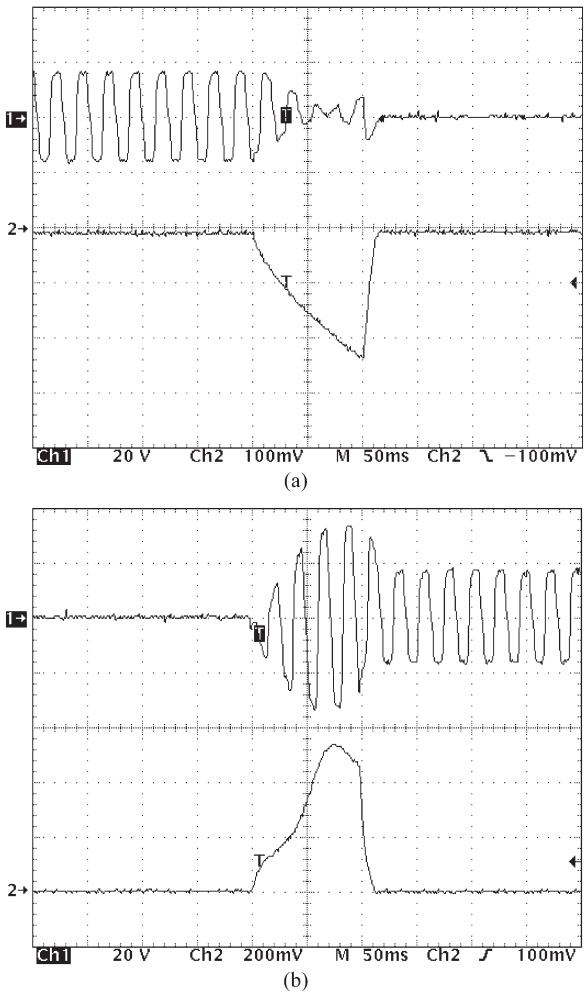

Fig. 18. Measured transient responses of no-load EMF during mode transitions at 100 r/min. (a) DSPM mode to SR mode (20 V/div, 1 A/div, and 50 ms/div). (b) SR mode to DSPM mode (20 V/div, 4 A/div, and 50 ms/div).

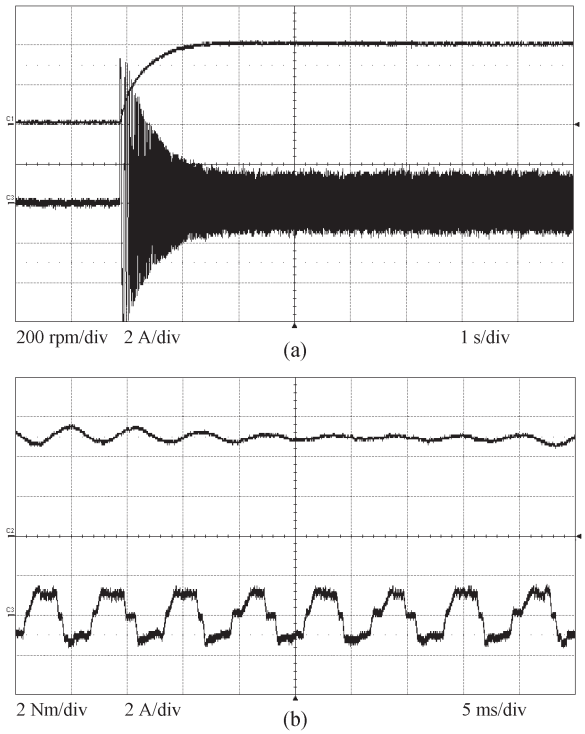

Fig. 19. Measured operating performances under DSPM mode. (a) Transient responses of rotor speed and armature current during startup (200 r/min/div, 2 A/div, and 1 s/div). (b) Steady-state waveforms of output torque and armature current at 400 r/min (2 N · m/div, 2 A/div, and 5 ms/div).

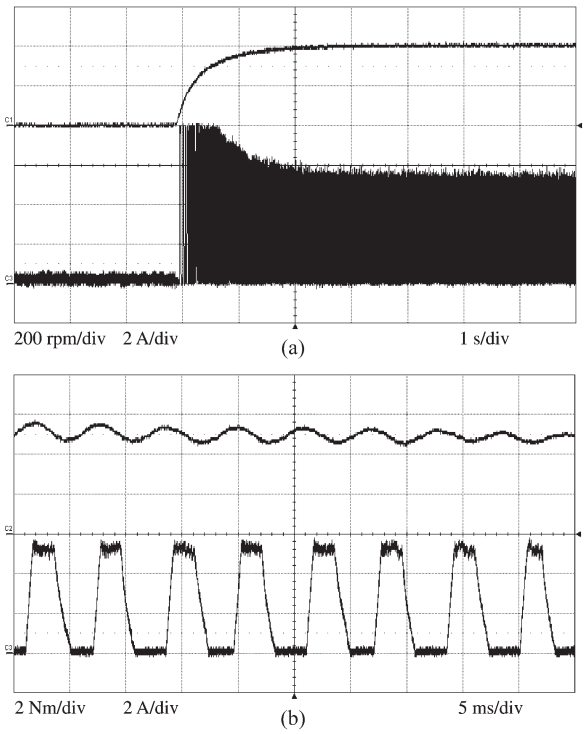

Fig. 20. Measured operating performances under SR mode. (a) Transient responses of rotor speed and armature current during startup (200 r/min/div, 2 A/div, and 1 s/div). (b) Steady-state waveforms of output torque and armature current at 400 r/min (2 N · m/div, 2 A/div, and 5 ms/div).

waveforms of output torque and armature current at the speed of 400 r/min are measured as shown in Figs. 19 and 20, respectively. As compared with the simulated results as shown in Figs. 15 and 16, the agreements are very good. It can be observed that the high-frequency torque ripple component as found in the simulation results is absent in the measured results. It is actually due to the fact that this high-frequency component is filtered inherently by the torsional damping effect

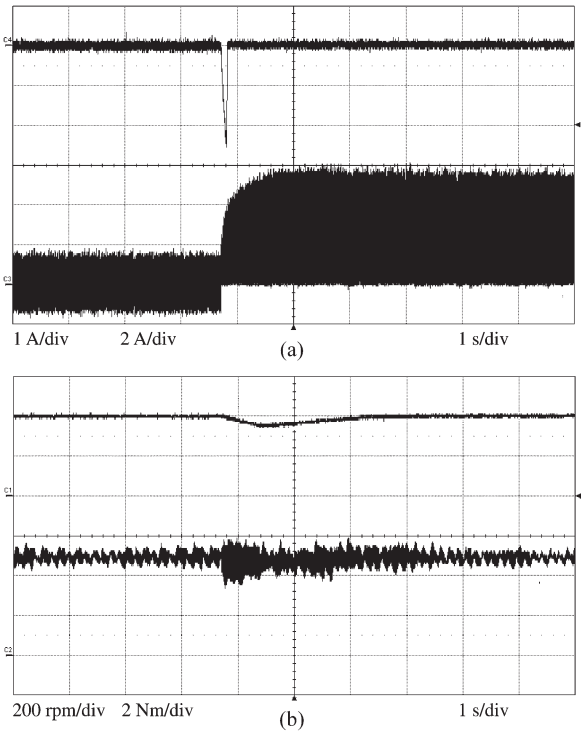

Fig. 21. Measured dynamic responses during transition from DSPM mode to SR mode at 400 r/min. (a) Demagnetizing current and armature current (1 A/div, 2 A/div, and 1 s/div). (b) Rotor speed and output torque (200 r/min, 2 N · m/div, and 1 s/div).

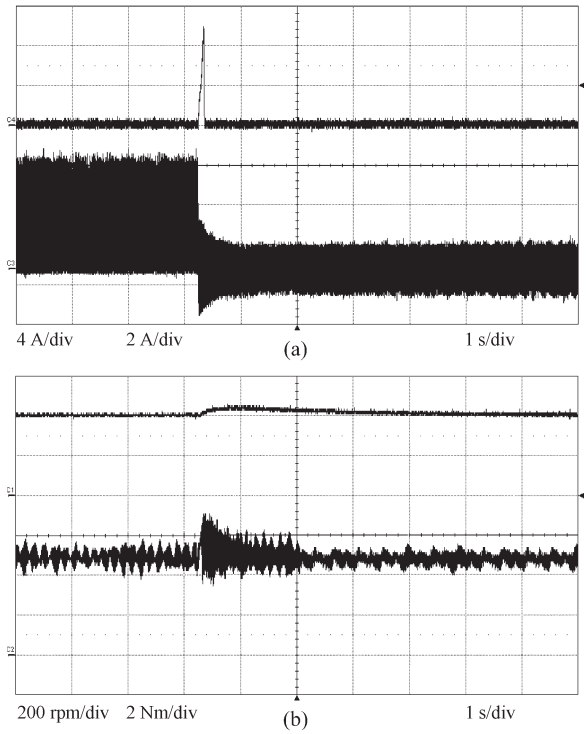

Fig. 22. Measured dynamic responses during transition from SR mode to DSPM mode at 400 r/min. (a) Magnetizing current and armature current (4 A/div, 2 A/div, and 1 s/div). (b) Rotor speed and output torque (200 r/min, 2 N · m/div, and 1 s/div).

of mechanical couplers. Defining the torque ripple factor as the peak-to-peak value to the average value, the measured torque ripple factor is 21.8% under the DSPM mode and 23.6% under the SR mode. This torque ripple value is similar to that of all kinds of doubly salient motors, including the SR motor which has been accepted for electric vehicle application. In addition, this torque ripple can be further reduced by properly optimizing the tooth dimensions or adopting rotor skewing [18].

Finally, the dynamic performances during mode transitions are evaluated. When the motor operates at the speed of 400 r/min under the DSPM mode, a negative current pulse is suddenly applied to completely demagnetize the PMs, hence switching to the SR mode of operation. The corresponding dynamic responses of demagnetizing current, armature current, rotor speed, and output torque are measured as shown in Fig. 21. Similarly, the dynamic responses during transition from the SR mode to the DSPM mode are also measured as shown in Fig. 22. Both of these responses verify that the proposed control scheme works properly, namely, the rotor speed can quickly settle at its commanded value and the output torque can be kept unchanged.

VI. Conclusion

In this paper, the dual-mode operation of the dc-excited memory motor under flux regulation has been proposed and implemented. The motor can operate either under the DSPM mode with bipolar armature current applied or under the SR mode with unipolar armature current applied. By utilizing the $\Psi - i$ diagram, the critical transition point between the DSPM mode and the SR mode has been determined, and an equivalent output torque can be maintained. Consequently, the operating performances of the motor under these two modes and during mode transitions have been evaluated. Both simulation and experimental results are given to verify the validity of the proposed dual-mode operation. Further work will be focused on quantitative comparison of the proposed machine with other PM machines under the same thermal condition.

References

[1] J. F. Gieras, *Motor Technology: Design and Application*. Boca Raton, FL: CRC Press, 2009.
[2] K. T. Chau, C. C. Chan, and C. Liu, "Overview of permanent-magnet brushless drives for electric and hybrid electric vehicles," *IEEE Trans. Ind. Electron.*, vol. 55, no. 6, pp. 2246–2257, Jun. 2008.
[3] T. M. Jahns, "Flux-weakening regime operation of an interior permanent-magnet synchronous motor drive," *IEEE Trans. Ind. Appl.*, vol. IA-23, no. 4, pp. 681–689, Jul. 1987.
[4] L. Xu, L. Ye, L. Zhen, and A. El-Antably, "A new design concept of permanent magnet machine for flux weakening operation," *IEEE Trans. Ind. Appl.*, vol. 31, no. 2, pp. 373–378, Mar./Apr. 1995.
[5] V. Ostovic, "Memory motors—A new class of controllable-flux permanent magnet machines for true wide-speed operation," *IEEE Ind. Appl. Mag.*, vol. 9, no. 1, pp. 52–61, Jan./Feb. 2003.
[6] T. J. E. Miller, *Switched Reluctance Motors and Their Control*. Oxford, U.K.: Magna Phys. Publ., 1993.
[7] C. Liu, K. T. Chau, J. Z. Jiang, and L. Jian, "Design of a new outer-rotor permanent magnet hybrid machine for wind power generation," *IEEE Trans. Magn.*, vol. 44, no. 6, pp. 1494–1497, Jun. 2008.
[8] W. Hua, M. Cheng, and G. Zhang, "A novel hybrid excitation flux-switching motor for hybrid vehicles," *IEEE Trans. Magn.*, vol. 45, no. 10, pp. 4728–4731, Oct. 2009.
[9] C. Yu, K. T. Chau, X. Liu, and J. Z. Jiang, "A flux-mnemonic permanent magnet brushless motor for electric vehicles," *J. Appl. Phys.*, vol. 103, no. 7, pp. 07F 103-1– 07F 103-3, Apr. 2008.
[10] C. Yu, K. T. Chau, and J. Z. Jiang, "A flux-mnemonic permanent magnet brushless machine for wind power generation," *J. Appl. Phys.*, vol. 105, no. 7, pp. 07F 114-1–07F 114-3, Apr. 2009.

[11] C. Yu and K. T. Chau, "Design, analysis and control of DC-excited memory motors," *IEEE Trans. Energy Convers.*, vol. 26, no. 2, pp. 479–489, Jun. 2011.
[12] C. Yu, X. Zhang, S. Gao, and D. Wu, "Comparison of permanent magnet brushless motors for electric vehicles," in *Proc. IEEE Veh. Power Propulsion Conf.*, Lille, France, Sep. 2010, pp. 1–5.
[13] C. Yu and K. T. Chau, "New fault-tolerant flux-mnemonic doubly-salient permanent-magnet motor drive," *IET Electr. Power Appl.*, vol. 5, no. 5, pp. 393–403, May 2011.
[14] D. A. Staton, W. L. Soong, and T. J. E. Miller, "Unified theory of torque production in switched reluctance and synchronous motors," *IEEE Trans. Ind. Appl.*, vol. 31, no. 2, pp. 329–337, Mar./Apr. 1995.
[15] Y. Liao, F. Liang, and T. A. Lipo, "A novel permanent motor with doubly salient structure," *IEEE Trans. Ind. Appl.*, vol. 31, no. 5, pp. 1069–1078, Sep./Oct. 1995.
[16] D. A. Staton, R. P. Deodhar, W. L. Soong, and T. J. E. Miller, "Torque prediction using the flux-MMF diagram in AC, DC, and reluctance motors," *IEEE Trans. Ind. Appl.*, vol. 32, no. 1, pp. 180–188, Jan./Feb. 1996.
[17] R. Krishnan, *Permanent Magnet Synchronous and Brushless DC Motor Drives*. Boca Raton, FL: CRC Press, 2009.
[18] Y. Gong, K. T. Chau, J. Z. Jiang, C. Yu, and W. Li, "Design of doubly salient permanent magnet motors with minimum torque ripple," *IEEE Trans. Magn.*, vol. 45, no. 10, pp. 4704–4707, Oct. 2009.

Chuang Yu received the B.Eng. and M.Eng. degrees in electrical engineering from Beijing Institute of Technology, Beijing, China, in 2004 and 2006, respectively, and the Ph.D. degree in electrical engineering from The University of Hong Kong, Pokfulam, Hong Kong, in 2010.

He is currently an Engineering Specialist with Johnson Electric, Shatin N.T., Hong Kong. His research interests include electric machine design, electric drives, renewable energy developments, and power electronics, particularly the design, analysis, and control of permanent-magnet brushless motors and flux switching motors.

K. T. Chau (M'89–SM'04) received the B.Sc. (Eng.) (first-class honors), M.Phil., and Ph.D. degrees in electrical and electronic engineering from The Univerisity of Hong Kong, Pokfulam, Hong Kong, in 1988, 1991, and 1993, respectively.

He is currently a Professor in the Department of Electrical and Electronic Engineering, The University of Hong Kong, where he is also the Director of the International Research Center for Electric Vehicles. His research interests include three main areas: electric vehicles, electric drives, and power electronics. In these areas, he has authored or coauthored more than 200 refereed technical papers. He is also the coauthor of a monograph, *Modern Electric Vehicle Technology* (Oxford University Press, 2001).

Prof. Chau is a Fellow of the Institute of Engineering and Technology, U.K. He was the recipient of the Outstanding Young Researcher Award in 2003, the University Teaching Fellowship Award in 2004, and the Award for Innovative Excellence in Teaching, Learning, and Technology in 2005.